

Modeling airflow-driven water droplet removal from a flat surface

TOBIAS DANCZUL¹, WOUTER HETEBRIJ², FAEZE KHALIGHI³, LUKAS KOGLER¹, DOMENICO LAHAYE⁴, ELLEN LUCKINS⁵, WIM MUNTERS³, MICHAEL NEUNTEUFEL¹, GUDMUND PAMMER⁶, KEES VUIK⁴, OLIVER WHITEHEAD⁵, YANG ZHOU⁷

Abstract

Motivated by the goal of removing small water droplets from semiconductor wafers, the ambition of this investigation is to analyze the behaviour of droplets adhered to a flat surface when exposed to different types of air flows. A sequence of models, increasing in both complexity and fidelity, is proposed to capture the setup. Capabilities and limitations of each modeling approach are demonstrated for representative example cases. Under mild assumptions, we propose a model order reduction that restricts omits the computation of the air flow, and restricts the computational domain to the interior of the droplet itself,

¹Technische Universität Wien, Austria

²Vrije Universiteit Amsterdam, The Netherlands

³Technische Universiteit Eindhoven, The Netherlands

⁴Technische Universiteit Delft, The Netherlands

⁵University of Oxford, United Kingdom

⁶Universität Wien, Austria

⁷University of Bath, United Kingdom

drastically accelerating computations. We finally highlight remaining difficulties and suggest concrete actions for future investigation.

KEYWORDS: COMPUTATIONAL FLUID DYNAMICS, DROPLETS, LUBRICATION THEORY, MULTIPHASE FLOW, NAVIER-STOKES EQUATIONS

6.1 Introduction

The company that suggested the herein considered problem is *VDL Enabling Technologies Group* (VDL ETG), which is part of the internationally operating *VDL Groep*. This is a subcontracting company specializing in metalworking, mechatronic systems and system supply, plastics processing and surface treatment. Their equipment is used in various processes such as vacuum process chambers, wafer stages and wafer handlers. The current treatment of the latter is cause for the collaboration with *SWI2020*.

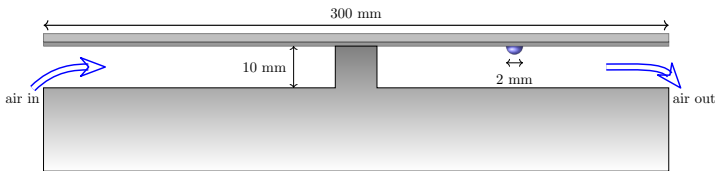


Figure 6.1: A pure water droplet is attached to the downward side of a semiconductor wafer. Typical dimensions and air-driven removal strategy are shown.

During wafer handling, the wafer is attached at its center, leaving a space between the bottom wafer surface and an underlying plate of up to 10 mm. In practice, small water droplets with volumes up to 10 mm^3 are often found attached on this bottom surface, as shown in Figure 6.1. This contamination impairs the processing of the current wafer, and could further contaminate subsequently processed ones. Due to technical constraints, wafer cleaning should be completed within a period of 10 seconds. However, the whole procedure takes place in a highly controlled environment which disallows many removal strategies

such as thermal treatment, application of electric fields, or addition of volatile solvents. This renders most standard cleaning methods infeasible.

The state-of-the-art method of tackling this issue is spinning the wafer. Due to the centrifugal force the water droplets are pushed outwards to the edge where they are aspirated and removed. VDL ETG currently considers a different approach: pushing the droplet along the surface to the edge by an imposed air flow. The investigation and optimization of this airflow-driven droplet removal is the subject of the current study.

The physics of flow-driven movement of droplets on flat surfaces has been the subject of various prior research efforts (see, e.g., Fan, Wilson, and Kapur (2011), Seevaratnam et al. (2010), and Grinats et al. (2019)), illustrating different modes of movements including sliding, oscillations, and droplet breakup for different combinations of droplet size and imposed airflow. An example of the former simple sliding regime is shown in Figure 6.2, which illustrates the position of a set of airblown droplets with different size as a function of time. It can be seen that droplet movement is highly dependent on size, as smaller droplets tend to move much slower and are hence harder to remove within a given time window. Given that strong airflows could cause the break-up of droplets, this observation illustrates the difficulty of the task at hand: the reduced volume and surface of broken droplets leads to a reduced force exerted by the flow, rendering these resulting droplets even harder to remove. Furthermore, the bottom plate could be contaminated by water resulting, eventually into a propagation onto subsequent wafers and worsening the situation. It is hence expected that there exists an optimal driving air velocity to remove droplets in minimal time without breakup. Moreover, given the frequent observation of droplet shape oscillations, not only the amplitude but also possible oscillations in the air flow might have effect on the droplet removal time. Indeed, oscillations could incite resonance modes in droplet shapes, thereby magnifying the drag force which is exerted by the air flow.

In this work, we investigate the droplet removal problem using mathematical models to increase the overall understanding of the problem and provide pathways to optimize the removal process. The manuscript is structured as follows. Firstly, Section 6.2 discusses the need for a

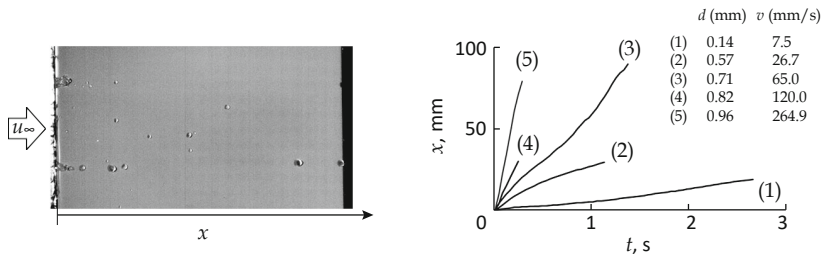


Figure 6.2: Experimental setup and results for droplets of varying size on flat surface blown by airflow of $u_\infty = 20$ m/s. *Left:* Topview setup photograph. *Right:* Droplet coordinates as a function of time. Figure adapted from Grinats et al. (2019).

modeling chain as opposed to a single model, and details the methodology and results of the mathematical models used in the current work. Next, Section 6.3 summarizes and compares the main findings from the different models. In closing, Section 6.4 formulates overall conclusions and provides concrete recommendations for further steps.

6.2 Modeling

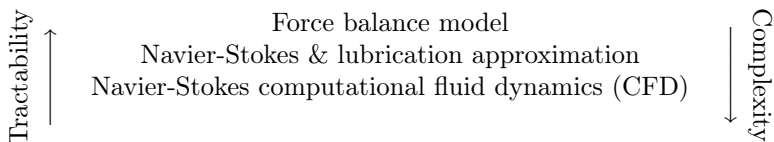
We consider the simplified situation in which a single water droplet is placed on the bottom of a flat surface (see Figure 6.3). The droplet is exposed to an airflow with freestream inlet speed u_∞ and the bottom wafer handler surface is neglected. Despite these simplifications, the physics of the resulting problem remain complex, i.e. it involves a wall-bounded multiphase free-surface flow which is inherently three-dimensional and unsteady. As a result, analytical solutions to detailed mathematical models can not be found. Furthermore, numerical solutions to such models, e.g. based on the three-dimensional unsteady Navier–Stokes equations, are intractable given the available time and computational resources in the current project. Instead, we consider different models with varying tractability, complexity and computational cost which also complement each other. Rather than making precise numerical comparisons between models or predictions for a spe-



Figure 6.3: Basic setup of a single droplet attached to a flat surface, blown by an imposed free-stream airflow u_∞ .

cific set of conditions, we choose to qualitatively assess and compare capabilities and limitations of each model. This allows us to identify most promising methods and provides ways to move forward in modeling and optimizing the droplet removal. Material properties used in each of the models detailed below are consistent with the problem description and summarized in Table 6.1.

The models considered in this manuscript are described below. In Section 6.2.1, a force-balance model is introduced. Next, Section 6.2.2, discussed a model based on a lubrication approximation of the Navier–Stokes equations. Finally, Section 6.2.3 elaborates on two models based on a computational fluid dynamics approach to the Navier–Stokes equations. The models can be ranked in terms of tractability and complexity as shown below:



6.2.1 Force balance model

In this section we describe an ordinary differential equation (ODE) model for the droplet velocity. This model was originally proposed in Grinats et al. (2019), where the droplet is assumed to be on the upper part of a smooth plate. In our report, we investigate the motion of a droplet with a volume $V = 7 \text{ mm}^3$ (corresponding to a spherical radius $a = 1.44 \text{ mm}$) attached to the bottom of the wafer (see Figure 6.4).

Table 6.1: Physical parameters and material properties used throughout this work.

Reference temperature	$T_r = 20^\circ\text{C}$
Water density	$\rho_w = 1000 \text{ kg/m}^3$
Water kinematic viscosity	$\nu_w = 1.004 \times 10^{-6} \text{ m}^2/\text{s}$
Water dynamic viscosity	$\mu = 1.002 \times 10^{-3} \text{ kg}/(\text{m} \cdot \text{s})$
Gas density	$\rho_g = 1.204 \text{ kg/m}^3$
Gas kinematic viscosity	$\nu_g = 1.82 \times 10^{-5} \text{ m}^2/\text{s}$
Water-Gas surface tension coefficient	$\sigma = 72.86 \times 10^{-3} \text{ N/m}$
Water-wafer equilibrium contact angle	$\theta = 45^\circ$
Gravitational acceleration	$g = 9.81 \text{ N/kg}$

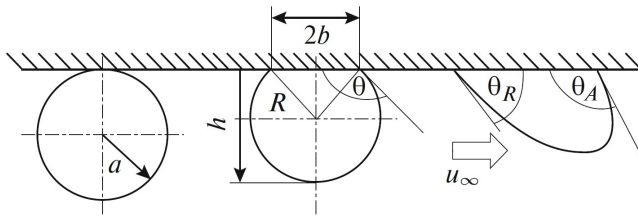


Figure 6.4: Geometrical representation of the droplet as part of a sphere above the plate. *Left:* Spherical droplet ($\theta = \pi$), *Middle:* Truncated droplet ($\theta \leq \pi$), *Right:* Deformed truncated droplet ($\theta_R \leq \theta_A \leq \pi$), blown by air flow with velocity u_∞ . Figure adapted from Grinats et al. (2019).

Model description

The droplet is assumed to behave like a single particle with mass m and velocity at time t denoted by $u(t)$. At rest, the droplet assumes the shape of a truncated sphere with contact angle $\theta = 45^\circ$. In response to the imposed airflow, the droplet will attain a deformed shape with different contact angles on the windward (θ_R) and leeward (θ_A) sides of the droplet. We consider the one-dimensional case where the velocity changes along the horizontal direction. Writing out a force balance for

the droplet, Newton's second law of motion dictates that

$$m \frac{du(t)}{dt} = F_a + F_\sigma + F_\mu, \quad (6.1)$$

where F_a , F_σ and F_μ denote the aerodynamic drag force, the surface tension force and the dissipative force, respectively. The aerodynamic force represents the push by the jet of air on the droplet and is given by

$$F_a = \frac{1}{2} C_D \rho_g S_\perp \|u_\infty - u(t)\| (u_\infty - u(t)), \quad (6.2)$$

where $C_D = 0.5$ is the drag coefficient Grinats et al. (2019), ρ_g is the density of the gas, S_\perp is the frontal area of the droplet, and u_∞ is the speed of the gas at the droplet boundary. The surface tension force F_σ resists the droplet motion and is given by

$$F_\sigma = -2b\sigma (\cos \theta_R - \cos \theta_A) \quad (6.3)$$

where $2b$ is the length of the contact line between the droplet and the wafer, and σ is the surface tension coefficient. Windward and leeward contact angles $\theta_R = 5^\circ$ and $\theta_A = 45^\circ$ are derived from ad-hoc tabulated experimental data for $\theta = 45^\circ$ Grinats et al. (2019). The friction force models loss of kinetic energy due to internal viscous dissipation and is assumed to be proportional to the droplet velocity $u(t)$, given by

$$F_\mu = -\mu \frac{\pi b^2}{h/2} u(t). \quad (6.4)$$

where μ is the viscosity of water. The gravitational force has no component in the direction of motion and can therefore be neglected. In the above equations, parameters R , h , b , and S_\perp are geometric features of the droplet shape (see Figure 6.4), which are computed as

$$R = \frac{a}{\left[1 - \frac{(1+\cos \theta)^2(2-\cos \theta)}{4}\right]^{1/3}}, \quad (6.5)$$

$$h = R(1 - \cos \theta), \quad (6.6)$$

$$b = R \sin \theta, \quad (6.7)$$

$$S_\perp = R^2 \left(\theta - \frac{\sin 2\theta}{2}\right). \quad (6.8)$$

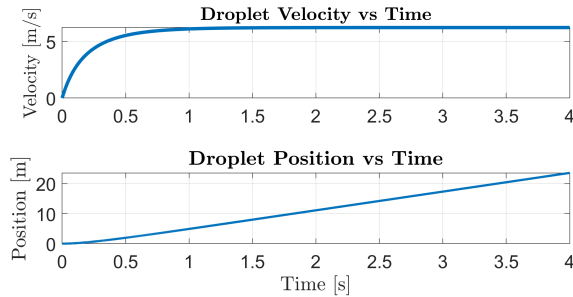


Figure 6.5: (Top) Computed velocity $u(t)$ vs Time (*seconds*). (Bottom) Computed displacement or Position (*m*) vs Time (*seconds*).

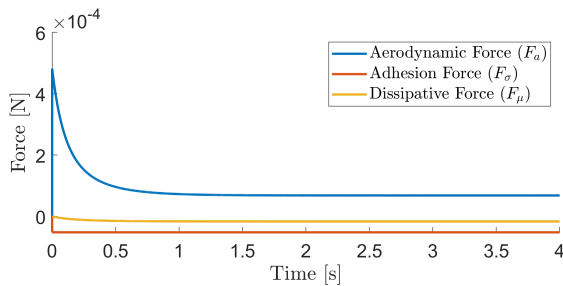


Figure 6.6: Computed force components F_a (blue), F_σ (orange) and F_μ (yellow).

Numerical results

The force balance model in Equation (6.1) is supplied with the droplet initial condition $u(0) = 0$ m/s, the air flow velocity with $u_\infty = 10$ m/s (boundary-layer effects are neglected) and integrated numerically using forward Euler.

In Figure 6.5, we see that under the influence of air flow, the droplet accelerates fast within the first 0.5 seconds, reaching a steady speed of 6.3 m/s. The model indicates that after 4 seconds, the droplet has travelled a distance over 20 meters. In Figure 6.6, the forces acting on

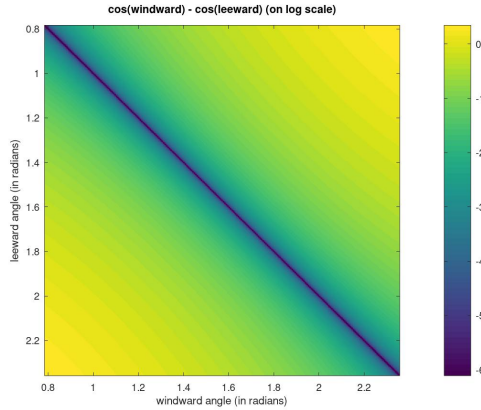


Figure 6.7: The function $\cos(\theta_R) - \cos(\theta_A)$ on the domain $\pi/4 \leq \theta_R, \theta_A \leq 3 * \pi/4$.

the droplet as it moves with the air flow are shown. From the graph, we can see that the aerodynamic force is big when the droplet is steady due to the large velocity difference $u_\infty - u(t)$. The surface tension force F_σ remains constant and, for the current setup, the friction force F_μ is significantly smaller than F_σ and F_a .

Comparing the current results to the indicative experimental data from Figure 6.2, we find that the force model overestimates droplet velocities by an order of magnitude. The main culprit behind this overestimation is the uncertainty on the tabulated data for the contact angle hysteresis $\cos(\theta_R) - \cos(\theta_A)$. Figure 6.7 shows the values that this hysteresis attains for angles between $\pi/4$ and $3\pi/4$, indicating that this parameter directly scales the main resistive force, i.e. the surface tension F_σ , by several orders of magnitude. By neglecting the dissipative friction force, which is justified for small $u(t)$, we can approximate the steady-state velocity U by expressing $du/dt = 0$, resulting in

$$U = u_\infty - \sqrt{\frac{4 b \sigma (\cos \theta_R - \cos \theta_A)}{C_D \rho_g S_\perp}}, \quad (6.9)$$

which shows the direct dependence of U on uncertain parameters θ_R and θ_A . Note also that C_D is highly dependent on the droplet shape.

In summary, the current model, despite being computationally inexpensive, is not suitable for quantitative predictions of droplet velocities. However, there is much room for improvement. For instance, an essential parameter that is not adequately modeled in the current approach is the shape of the moving droplet, as evidenced by the argumentation above. This motivates the development and application of more advanced models as shown in the following paragraph. The inclusion of shape parametrizations from more detailed models into the force balance model could lead to a very computationally efficient model with increased accuracy over the current one. This is however out of scope of the current investigation and left for future work.

6.2.2 Navier–Stokes model with lubrication approximation

In this section we present a second model for the motion of the water droplet due to an air flow. This model is based on the Navier-Stokes equations for the fluid flow within the water droplet, which we reduce using the lubrication approximation.

Model description

In this section we work in 2D for simplicity, but the same methods extend easily to 3D. The droplet of water occupies the region between $z = h(x, t)$ (the air-water interface) and $z = 0$ (the wafer) in Figure 6.9. The region $z < h(x, t)$ is occupied by the air. The droplet shape h is a free boundary to be solved for as part of the solution of our model. The dimensionless incompressible Navier-Stokes equations for the water velocity, \mathbf{u} , and pressure, p , in $h(x, t) < z < 0$ are

$$\nabla \cdot \mathbf{u} = 0, \quad (6.10)$$

$$\text{Re} \frac{\partial \mathbf{u}}{\partial t} = -\nabla p + \nabla^2 \mathbf{u}, \quad (6.11)$$

where $\text{Re} = U_w d / \nu_w$ is the Reynolds number of the flow, with d the droplet diameter and U_w a typical water velocity. The overall pressure

is $P = p - \text{Ca}^{-1} \text{Bo} \mathbf{e}_z$, so that the hydrostatic term is absorbed into p in (6.11). On the $z = 0$ boundary we have no slip so that $\mathbf{u} = \mathbf{0}$. On $z = h(x, t)$ we have the boundary conditions

$$\frac{\partial}{\partial t}(z - h) = 0, \quad (6.12)$$

$$[\mathbf{n} \cdot \underline{\boldsymbol{\sigma}} \mathbf{n}]_{\pm}^{\pm} = \text{Ca}^{-1} (\kappa + \text{Bo} h), \quad (6.13)$$

$$[\mathbf{t} \cdot \underline{\boldsymbol{\sigma}} \mathbf{n}]_{\pm}^{\pm} = 0, \quad (6.14)$$

which are the kinematic condition, and the normal and tangential stress balances across the interface. Here, κ is the dimensionless surface curvature, \mathbf{n} and \mathbf{t} are unit normal and tangent vectors to the interface,

$$\sigma_{ij} = -P\delta_{ij} + \left(\frac{\partial u_i}{\partial x_j} + \frac{\partial u_j}{\partial x_i} \right), \quad (6.15)$$

and

$$\text{Ca} = \frac{\mu_w U_w}{\gamma}, \quad \text{Bo} = \frac{\rho_w g d^2}{\gamma}, \quad (6.16)$$

are the capillary and Bond numbers respectively. In particular, assuming $d \sim 10^{-3} \text{m}$ and $U_w \sim 10 \text{ms}^{-1}$ we expect

$$\text{Ca} \approx 0.1, \quad \text{Bo} \approx 0.1. \quad (6.17)$$

We assume the air in $z < h(x, t)$ also satisfies the Navier-Stokes equations, although with much higher Reynolds number, and negligible gravitational force. The water and air flows are coupled through the force balance boundary conditions (6.13)-(6.14) at $z = h$. The thesis Fry (2011) is a thorough asymptotic examination of the shearing interaction between an air flow over a (stationary) droplet on a substrate. In Fry (2011), the shear effect of the air on the water droplet (sitting on top of the substrate rather than below) causes its shape to deform, while the droplet in turn causes a perturbation to the Blasius boundary layer air flow. The two flows are therefore fully coupled, and the asymptotic approach therefore requires full Triple-Deck theory, with extensions. Fry (2011) do not consider the movement of droplets across

the substrate due to the air flow, only the deformation of stationary drops.

While the full coupled problem should be considered for more accurate results, for simplicity in this study group, we assume that the droplet shape has negligible effect on the air flow, and so only consider the shearing effect of a prescribed air flow on the droplet. The air flow in the boundary layer is assumed to be linear shear flow $U_a = -az$, for $z < 0$, so that the shear stress $f = -a$ is constant, which we assume is known. Greater values of $a > 0$ indicate greater velocity air flows.

Lubrication approximation We assume we have a small aspect ratio $\delta = [h]/[x]$, and so make the lubrication approximation:

$$\delta \ll 1 \qquad \text{Re}\delta^2 \ll 1 \qquad (6.18)$$

to simplify the system (6.10)-(6.14). With this assumption we can reduce the problem to a single equation for the droplet boundary h in terms of the prescribed shear stress f , namely:

$$h_t = \left(\frac{h^3}{3\text{Ca}} (h_{xxx} + \text{Bo}h_x) \right)_x - \left(\int_0^h \int_0^z f \hat{z} dz \right)_x, \qquad (6.19)$$

or, with constant shear $f = -a$,

$$h_t = \left(\frac{h^3}{3\text{Ca}} (h_{xxx} + \text{Bo}h_x) \right)_x + \left(\frac{ah^2}{2} \right)_x. \qquad (6.20)$$

Travelling wave assumption As we have seen in the experimental indicative results (Figure 6.2), and the force balance model (Figure 6.5), the droplet reaches a constant velocity almost instantaneously. Hence, we make the assumption that the droplet has a steady shape and constant velocity U to be determined. That is, we make the travelling wave Ansatz, changing variables to

$$\xi = x - Ut, \qquad H(\xi) = h(x, t).$$

Thus Equation 6.20 reduces to the fourth order ODE

$$-UH_\xi = \left(\frac{H^3}{3\text{Ca}} (H_{\xi\xi\xi} + \text{Bo}H_\xi) \right)_\xi + \left(\frac{aH^2}{2} \right)_\xi. \qquad (6.21)$$

Integrating with respect to ξ , and assuming that the droplet has a finite length, so that there is a ξ such that $H(\xi) = 0$, we have the third order ODE

$$-UH = \frac{H^3}{3\text{Ca}} (H_{\xi\xi\xi} + \text{Bo}H_{\xi}) + \frac{aH^2}{2}. \quad (6.22)$$

Boundary conditions To close the problem (6.22) for H , we require the four boundary conditions

$$H(0) = 0 = H(L), \quad H_{\xi}(0) = -\tan(\theta_1) \quad H_{\xi}(L) = \tan(\theta_2), \quad (6.23)$$

where $\xi = 0$ and L (TBD) are the endpoints of the droplet, and θ_1 and θ_2 are the contact angles at these endpoints respectively. The length L of the droplet is fixed by prescribing the total droplet volume

$$V = - \int_0^L H(\xi) d\xi. \quad (6.24)$$

We choose to use the Cox-Voinov model Cox (1986) for the movement of the contact lines in terms of the contact angles, setting

$$U = K (\theta_R^3 - \theta_1^3), \quad U = K (\theta_2^3 - \theta_A^3), \quad (6.25)$$

where θ_R and θ_A are the receding and advancing contact angles, respectively, which are experimentally determined constants for the substrate/fluid/gas combination. Here K is an order 1 constant. Equations (6.22)-(6.25) form a closed system for $H(\xi)$, U , L , θ_1 and θ_2 .

Numerical results

We numerically solve the boundary value problem (6.22)-(6.25), in MATLAB, using inbuilt solver 'bvp4c'. We change variables $\xi = LX$ in order to solve on the fixed domain $X \in [0, 1]$, and write the integral constraint (6.24) in differential form by introducing the new variable $Y(X)$, the solution of

$$Y'(X) = -LY(X), \quad Y(0) = 0, \quad Y(1) = V, \quad (6.26)$$

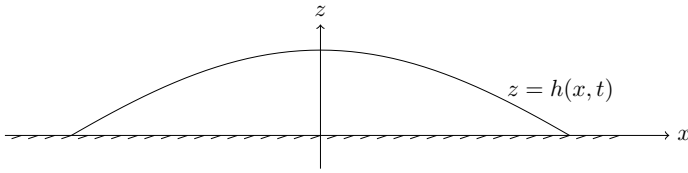


Figure 6.8: A schematic diagram of the set up in Fry (2011).

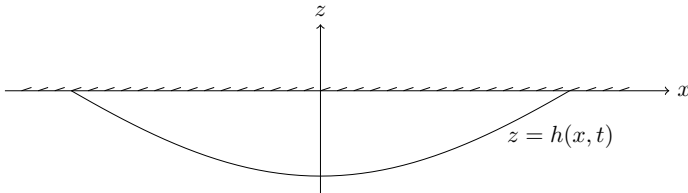


Figure 6.9: A schematic diagram of the set up in our problem.

which we solve simultaneously with (6.22). We investigate the influence of increasing the inlet air velocity, which is equivalent in our model to increasing the shear a on the droplet.

As can be observed in Figure 6.10, the droplet speed $U \sim 0.1$, indicating (by our choice of nondimensionalisation) that the fluid circulation within the droplet is around an order of magnitude below the droplet speed. Initially the droplet speed varies linearly with the inlet air velocity, whereas the length of the droplet is largely unaffected. However, at an air shear stress of more than $a_{\text{crit}} \approx 4$, the droplet length increases rapidly, while the increase of the droplet speed decreases. At this critical value we see a dramatic change in the droplet profile: for a, a_{crit} the droplet shape is slightly deformed by the air shear, but for $a > a_{\text{crit}}$ the shape is altered drastically, with a single drop trailing a long tail. We might expect that such long, thin tails might in reality break up into smaller droplets, a phenomenon not possible within this model.

We also investigate the effect of droplet volume on velocity. In Figure 6.11, we show the droplet lengths and velocities as the droplet volume - or in fact, area, in this 2D model - for fixed air shear a . We observe a fractional power law relating both U and V , and L with V ,

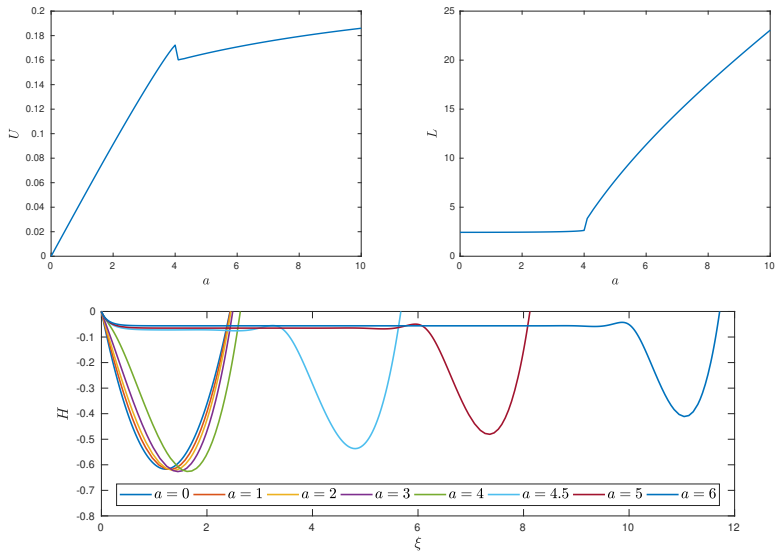


Figure 6.10: The dimensionless droplet speed U (top left), length L (top right), and profile $H(\xi)$ (bottom) of the droplet as shear due to air flow a varies. Here we have used $V = 1$, $\text{Bo} = 0.1$, $\text{Ca} = 0.1$, $\theta_A = \theta_R = \pi/4$, and $K = 0.44$.

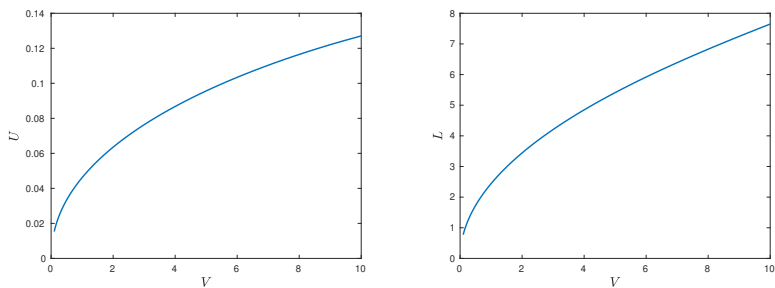


Figure 6.11: The dimensionless droplet speed U (left), length L (right), as the droplet volume V varies. Here we have used $a = 2$, $\text{Bo} = 0.1$, $\text{Ca} = 0.1$, $\theta_A = \theta_R = \pi/4$, and $K = 0.44$.

so that droplets with smaller volume travel at much smaller velocities. This is as expected from the experimental observations in Figure 6.2.

Summary

The model used in this section includes variations in the droplet shape at a computational cost which is only marginally higher than the force balance model from Section 6.2.1. The model may easily be extended to 3D, where a similar equation to (6.19) for h may be derived. This model also has the benefit of a systematic derivation from first principles, and so is expected to be accurate within the correct parameter regime. However, whether the situation of interest fits within the scope of this model is another question: in order that (6.18) hold we may only be able to model relatively slow air flows; and in particular, it is likely that the droplet shape impacts the air flow, so that the two flows should be fully coupled as in Fry (2011).

The observations from this model suggest that there exists an optimal inlet air flow with shear $a = a_{\text{crit}}$ to remove the droplets, maximizing droplet velocities without causing droplet breakup. It reiterates the requirement of avoiding droplet break-up at all costs. However, the current model does not allow us to accurately determine when or how droplet breakup occurs.

The limitations of the current model hence motivate the application of models that attempt to directly solve the Navier–Stokes governing equations with minimal a priori approximations. Such models are the subject of the following section.

6.2.3 Full Navier–Stokes models

In the current section, we use computational fluid dynamics (CFD) models to directly solve the droplet movement problem with minimal a priori approximations. The resulting governing equations are the full Navier–Stokes partial differential equations (PDEs), which are discretized in space and time. Although this PDE approach increases the overall model fidelity, it does render the current simulations orders of magnitude more costly than the previous ones based on low-dimensional ODEs. To reduce the computational cost, the dimensionality of the

models will still be reduced as detailed below. Furthermore, due to the complexity of building Navier–Stokes solvers from scratch, we resort to using open-source software packages.

Model description

There is a large body of literature that suggests different approaches to simulate problems similar to the one considered here, see e.g., Seevaratnam et al. (2010), Reusken, Xu, and Zhang (2015), and Ding and Spelt (2007). First and foremost, the resolution of the interface between the liquid water phase and the gaseous air phase turns out to be one of the most challenging aspects.

There are two different approaches how to address this problem, interface-capturing and interface-tracking simulations. Interface-capturing models incorporate an additional equation that describes the behaviour of the interface in time. A widely used interface-capturing model is the volume of fluid method (VOF) Hirt and Nichols (1981). The method is based on an indicator function which tracks the fraction of each respective phase throughout the domain. The interface is understood as diffusive transition between fluid and gas. This manipulation allows approximation of the discontinuity across the interface with continuous functions. The resolution of the layer between the two media, however, becomes computationally expensive as its width decreases. In contrast, interface-tracking simulations refrain from posing an additional equation to describe the transition between gas and fluid. Instead, they treat the behaviour of the interface implicitly, see e.g., Reusken, Xu, and Zhang (2015). In the current work, we consider both an interface-capturing approach, for which we use the OpenFOAM software⁸ in two-dimensional cases, and an interface-tracking approach, for which we use the NGSolve software⁹ in two- and three-dimensional cases.

Interface-capturing approach using OpenFOAM

In the interface-capturing approach we use a VOF method for free-surface flows Hirt and Nichols (1981). The governing equations are as

⁸<https://www.openfoam.com/>

⁹www.ngsolve.org

follows:

$$\frac{\partial \rho \mathbf{u}}{\partial t} + \nabla \cdot (\rho \mathbf{u} \mathbf{u}) = -\nabla p + \nabla \cdot (\mu \operatorname{sym}(\nabla \mathbf{u})) + \sigma \kappa \nabla \alpha + \rho \mathbf{g}, \quad (6.27)$$

$$\frac{\partial \alpha}{\partial t} + \nabla \cdot (\mathbf{u} \alpha) = 0, \quad (6.28)$$

$$\nabla \cdot \mathbf{u} = 0. \quad (6.29)$$

In these equations $\mathbf{u}(\mathbf{x}, t)$ and $p(\mathbf{x}, t)$ are the velocity and pressure fields respectively, and $\mathbf{g} = -g\mathbf{e}_3$ is the gravitational acceleration. In the VOF approach, two immiscible fluids (i.e. air in the gas phase and water in the liquid phase) are considered as one effective fluid throughout the simulation domain, the properties of which are calculated as a weighted average of both phases through the use of an indicator function $\alpha(\mathbf{x}, t)$. This function represents the volume fraction of the liquid water phase throughout the domain, and hence attains values $0 \leq \alpha \leq 1$. The density of the multiphase fluid can hence be expressed as $\rho = \alpha \rho_w + (1 - \alpha) \rho_a$, with ρ_w and ρ_a the density of the liquid water and gaseous air phase respectively. The viscosity throughout the domain is defined in an analogous way. The surface tension is modeled as $\sigma \kappa \nabla \alpha$, where σ is the surface tension constant, and $\kappa = -\nabla \cdot \frac{\nabla \gamma}{|\nabla \gamma|}$ is the curvature of the water-air interface. Material parameters are summarized above in Table 6.1.

The system of equations is numerically simulated using the `interFoam` solver of the open source OpenFOAM package. The equations are discretized using a second-order finite volume method. Time integration is performed using a standard explicit Euler integrator, and pressure-velocity coupling is attained using the PIMPLE algorithm. Further details on the numerics of `interFoam` can be found, for instance, in Deshpande, Anumolu, and Trujillo (2012).

Interface-tracking approach: NGSolve

In the interface-tracking approach, we consider a sharp interface model that has been introduced in Reusken, Xu, and Zhang (2015). We recap the most important results in the three-dimensional setting. The equations shall be understood in two dimensions respectively.

Throughout what follows, we consider a two-phase flow in a prismatic domain $\Omega \subset \mathbb{R}^d$, $d = 2, 3$, with liquid and gas medium $\Omega_1(t), \Omega_2(t) \subset \Omega$, respectively (see Figure 6.12). The evolving sharp interface between these two components is denoted by $\Gamma(t) := \overline{\Omega}_1(t) \cap \overline{\Omega}_2(t)$. We assume that both $\Omega_1(t)$ and $\Omega_2(t)$ are in contact with a part of the border, which we refer to as “sliding wall” $\partial\Omega_s \subset \partial\Omega$. The contact line $L(t)$ refers to that line where gas, fluid, and $\partial\Omega_s$ intersect. The normals on Γ and $\partial\Omega_s$ are referred to as \mathbf{n}_Γ and \mathbf{n}_s , respectively. The propagation of this system in terms of the unknown velocity $\mathbf{u}(\mathbf{x}, t)$ and the pressure $p(\mathbf{x}, t)$ are specified by the following system of partial differential equations.

$$\begin{cases} \rho_i \left(\frac{\partial \mathbf{u}}{\partial t} + \mathbf{u} \cdot \nabla \mathbf{u} \right) = \nabla \cdot \boldsymbol{\sigma}_i + \rho_i \mathbf{g}, \\ \nabla \cdot \mathbf{u} = 0, \\ \boldsymbol{\sigma}_i = \mu \operatorname{sym}(\nabla \mathbf{u}) + p_i \mathbf{I}, \end{cases} \quad \text{in } \Omega_i(t), \quad i = 1, 2, \quad (6.30a)$$

$$[\boldsymbol{\sigma} \mathbf{n}_\Gamma] = \nabla \cdot \boldsymbol{\sigma}_\Gamma, \quad V_\Gamma = \mathbf{u} \cdot \mathbf{n}_\Gamma, \quad [\mathbf{u}] = 0 \quad \text{on } \Gamma(t), \quad (6.30b)$$

$$\begin{cases} (\mathbf{I} - \mathbf{P}_s) \mathbf{u} = 0, \\ \mathbf{f}_s = \mathbf{P}_s \boldsymbol{\sigma} \mathbf{n}_s, \end{cases} \quad \text{on } \partial\Omega_s, \quad (6.30c)$$

$$\mathbf{f}_L = \mathbf{P}_s \boldsymbol{\sigma}_\Gamma \boldsymbol{\tau}_L, \quad \text{in } L(t), \quad i = 1, 2, \quad (6.30d)$$

$$\mathbf{u} = 0, \quad \text{on } \partial\Omega_D. \quad (6.30e)$$

Equations (6.30a) refer to the Navier-Stokes equations and models the flow of Ω_1 (liquid phase) and Ω_2 (gaseous phase) in the channel. Interface conditions are posed in Equation 6.30b, ensuring balancing of the forces on the interface, immiscibility of the mediums and its no-slip constraint. Here, $\boldsymbol{\sigma}_\Gamma = \tau(\mathbf{I} - \mathbf{n}_\Gamma \mathbf{n}_\Gamma^T) =: \tau \mathbf{P}_\Gamma$ refers to the interface stress tensor, with τ and V_Γ denoting the surface tension coefficient and the normal velocity of the interface, respectively. (6.30c) describes the usual Navier slip boundary condition on $\partial\Omega_s$ by means of the orthogonal projection $\mathbf{P}_s := \mathbf{I} - \mathbf{n}_s \mathbf{n}_s^T$ and a prescribed so-called *effective wall force* $\mathbf{f}_s = -\beta_s \mathbf{P}_s \mathbf{u}$. The force balance on the contact line is enforced by Equation 6.30d with $\boldsymbol{\tau}_L := \frac{\mathbf{P}_\Gamma \mathbf{n}_s}{\|\mathbf{P}_\Gamma \mathbf{n}_s\|}$, denoting the normal to L that is tangential to Γ . Here, $\mathbf{f}_L = -\beta_L (\mathbf{u} \cdot \mathbf{n}_L) \mathbf{n}_L + \tau \cos \theta_e \mathbf{n}_L$ is the *effective contact line force*. Homogeneous Dirichlet boundary conditions are prescribed on Ω_D .

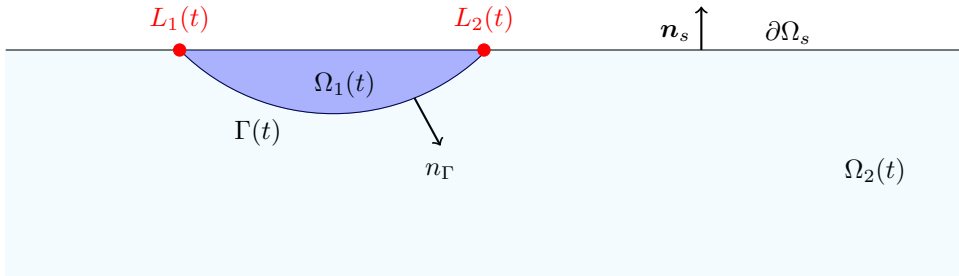


Figure 6.12: Initial configuration of the droplet in the two-dimensional setting.

The Navier-Stokes equations are given in Eulerian form, where the fluid particles are not associated with a finite element grid. The interface particles, however, must be resolved by the grid and thus, a Lagrangian description form is better suited. This would lead to mesh distortions as the interface might move in time. One could use XFEM or CutFem techniques or the Arbitrary Lagrangian Eulerian (ALE) description form Donea et al. (2004). Therefore, the current configuration $\Omega(t)$ is transformed to a fixed reference configuration, the initial configuration $\hat{\Omega} := \Omega(0)$. With the function

$$\Phi : \hat{\Omega} \times [0, T] \rightarrow \Omega(t) \times [0, T], \quad (\hat{\mathbf{x}}, t) \mapsto \Phi(\hat{\mathbf{x}}, t) = (\mathbf{d}(\hat{\mathbf{x}}, t), t) = (\mathbf{x}, t), \quad (6.31)$$

where \mathbf{d} is called the deformation function and its time derivative $\dot{\mathbf{d}} := \partial_t \mathbf{d}$ the mesh velocity. A function $f : \Omega(t) \times [0, T] \rightarrow \mathbb{R}^d$ on the current configuration is coupled with a function $\hat{f} : \hat{\Omega} \times [0, T] \rightarrow \mathbb{R}^d$ by the relation $f \circ \Phi = \hat{f}$ and there hold the following identities for the derivatives

$$\nabla_x f \circ \Phi \nabla_{\hat{\mathbf{x}}} \mathbf{d} = \nabla_{\hat{\mathbf{x}}} \hat{f}, \quad (6.32a)$$

$$\frac{\partial f}{\partial t} \circ \Phi = \partial_t \hat{f} - \nabla_{\hat{\mathbf{x}}} \hat{f} \mathbf{F}^{-1} \dot{\mathbf{d}}, \quad (6.32b)$$

where $\mathbf{F} := \nabla_{\hat{\mathbf{x}}} \mathbf{d}$ denotes the deformation gradient of \mathbf{d} . The deformation \mathbf{d} is related to Equation 6.30 by $\dot{\mathbf{d}} = V_\Gamma$ on the interface Γ , i.e.,

we have to extend the deformation to the domains with an auxiliary Poisson-like problem.

In order to make the above system of equations amenable to finite element discretization, we multiply each equation with test functions, integrate over the domain, followed by integration by parts and incorporate interface- and boundary conditions to arrive at the following weak formulation, see Reusken, Xu, and Zhang (2015) for further details: Find $\mathbf{u} \in \mathbf{V}$, $p \in Q$, $\mathbf{d}, \dot{\mathbf{d}} \in \mathbf{D}$ such that (for almost all) $t \in [0, T]$

$$\left\{ \begin{array}{l} m(\mathbf{d}; \partial_t \mathbf{u}, \mathbf{v}) + c(\mathbf{u} - \dot{\mathbf{d}}; \mathbf{u}, \mathbf{v}) + a(\mathbf{d}; \mathbf{u}, \mathbf{v}) + b(\mathbf{d}; \mathbf{v}, p) = \\ \quad f_{\text{ext}}(\mathbf{d}; \mathbf{v}) + f_{\Gamma}(\mathbf{d}; \mathbf{u}, \mathbf{v}) + f_L(\mathbf{d}; \mathbf{v}), \quad \forall \mathbf{v} \in \mathbf{V}, \\ b(\mathbf{d}; \mathbf{u}, q) = 0, \quad \forall q \in Q, \end{array} \right. \quad (6.33)$$

$$K(\dot{\mathbf{d}}, \mathbf{w}) = 0, \quad \forall \mathbf{w} \in \mathbf{D}, \quad (6.34)$$

under the constraints that $\dot{\mathbf{d}} = V_{\Gamma}$ on $\hat{\Gamma}$ and $\mathbf{d}(t) = \text{id} + \int_0^t \dot{\mathbf{d}}(s) ds$. The corresponding function spaces are defined by

$$\mathbf{V} := \{\mathbf{v} \in [H^1(\hat{\Omega})]^d : \mathbf{v} = 0 \text{ on } \partial\hat{\Omega}_D, (\mathbf{I} - \hat{\mathbf{P}}_s)\mathbf{v} = 0 \text{ on } \partial\hat{\Omega}_s\},$$

$$Q := L_2(\hat{\Omega}),$$

$$\mathbf{D} := \{\mathbf{d} \in [H^1(\hat{\Omega})]^d : \mathbf{d} = 0 \text{ on } \partial\hat{\Omega}\}.$$

The bilinear forms read as

$$m(\mathbf{d}; \mathbf{u}, \mathbf{v}) := \int_{\hat{\Omega}} J \rho \mathbf{u} \cdot \mathbf{v} dx,$$

$$\begin{aligned} a(\mathbf{d}; \mathbf{u}, \mathbf{v}) &:= \int_{\hat{\Omega}} J \mu \text{sym}(\nabla \mathbf{u} \mathbf{F}^{-1}) : \text{sym}(\nabla \mathbf{v} \mathbf{F}^{-1}) + \int_{\partial\hat{\Omega}_s} J \beta_s \hat{\mathbf{P}}_s \mathbf{u} \cdot \hat{\mathbf{P}}_s \mathbf{v} ds \\ &+ \int_{\hat{L}} J \beta_L \mathbf{u} \cdot \mathbf{n}_L \circ \mathbf{d} \mathbf{v} \cdot \mathbf{n}_L \circ \mathbf{d} d\gamma, \end{aligned}$$

$$b(\mathbf{v}, q) := - \int_{\hat{\Omega}} J (\text{tr}(\nabla \mathbf{v} \mathbf{F}^{-1}) q) dx, \quad c(\mathbf{w}, \mathbf{u}, \mathbf{v}) := \int_{\hat{\Omega}} J \rho (\mathbf{w} \cdot \nabla) \mathbf{u} \mathbf{F}^{-1} \cdot \mathbf{v} dx,$$

$$f_{\text{ext}}(\mathbf{v}) := \int_{\hat{\Omega}} J \rho \mathbf{g} \cdot \mathbf{v} dx, \quad f_{\Gamma}(\mathbf{u}, \mathbf{v}) := - \int_{\hat{\Gamma}} J \tau \mathbf{P}_{\Gamma} \circ \mathbf{d} : \nabla_{\hat{\Gamma}} \mathbf{v} \mathbf{F}^{\dagger} ds,$$

$$f_L(\mathbf{v}) := \cos \theta_c \int_{\hat{L}} J \tau \mathbf{v} \cdot \mathbf{n}_L \circ \mathbf{d} d\gamma,$$

$$K(\mathbf{d}, \mathbf{w}) := \int_{\Omega} \text{sym}(\nabla \mathbf{d}) : \text{sym}(\nabla \mathbf{w}) \, dx.$$

Here, J denotes, depending on the type of integral, the transformation determinant, $J = \det \mathbf{F}$, $J = \|\text{cof}(\mathbf{F})\|$, $J = \|\mathbf{F}\hat{\tau}\|$, and \mathbf{F}^\dagger the Moore-Penrose pseudo inverse. There holds

$$\begin{aligned} \mathbf{P}_\Gamma \circ \mathbf{d} &= \mathbf{I} - \mathbf{n}_\Gamma \circ \mathbf{d} \mathbf{n}_\Gamma \circ \mathbf{d}^T, & \mathbf{n}_\Gamma \circ \mathbf{d} &= \frac{\text{cof}(\mathbf{F})\hat{\mathbf{n}}_\Gamma}{\|\text{cof}(\mathbf{F})\hat{\mathbf{n}}_\Gamma\|}, & \mathbf{n}_s &= \hat{\mathbf{n}}_s, & \mathbf{P}_S &= \hat{\mathbf{P}}_S, \\ \mathbf{n}_L \circ \mathbf{d} &= \frac{\mathbf{P}_S \circ \mathbf{d}(\mathbf{n}_\Gamma \circ \mathbf{d})}{\|\mathbf{P}_S \circ \mathbf{d}(\mathbf{n}_\Gamma \circ \mathbf{d})\|}. \end{aligned}$$

The solving algorithm for one time step reads: For given \mathbf{d}^n , $\dot{\mathbf{d}}^n$, \mathbf{u}^n

1. Solve (6.30) with the old deformation and obtain \mathbf{u}^{n+1}
2. Set $\dot{\mathbf{d}}^{n+1} = \mathbf{u}^{n+1}$ on Γ and extend $\dot{\mathbf{d}}^{n+1}$ to the whole domain by solving a Poisson problem.
3. Compute $\mathbf{d}^{n+1} = \mathbf{d}^n + (t^{n+1} - t^n)\dot{\mathbf{d}}^{n+1}$

It should be mentioned that this approach cannot handle topological changes to the computational domain such as would be induced by droplet breakup. When approaching a state where droplet breakup should occur, the simulation becomes more and more unstable and eventually explodes. As we are explicitly interested in preventing droplet breakup in the first place, this is not a major concern.

Having this model at hand, we emphasize that discretization of the channel, even in the two-dimensional case, is computationally expensive, regarding the fact that only the behaviour of the droplet itself is of interest. To address this difficulty, we omit discretizing the air flow and instead prescribe the force of the air stream directly to the droplet in terms of suitable boundary conditions. This elimination of the exterior domain yields a drastic reduction in degrees of freedoms. An additional benefit of neglecting the air domain is a significantly higher mesh-quality, since the moving droplet mesh droplet no longer interacts with the static air domain mesh. This approach is described more precisely in the following.

Assuming air as a perfect gas, only pressure forces are induced on the interface Γ by the momentum $p = \rho(\mathbf{u}_\infty \cdot \mathbf{n}_\Gamma)\mathbf{n}_\Gamma$ and thus, $\boldsymbol{\sigma}_{\text{air}} = p\mathbf{I}$ and the right-hand side reads

$$f_{\text{ext}}(\mathbf{v}) = \int_{\hat{\Omega}} J\rho\mathbf{g} \cdot \mathbf{v} \, dx + \int_{\hat{\Gamma}_{\text{in}}} J\rho_{\text{air}}\mathbf{u}_\infty \cdot \mathbf{n}_\Gamma \circ \mathbf{d}\mathbf{v} \cdot \mathbf{n}_\Gamma \circ \mathbf{d} \, ds, \quad (6.35)$$

where $\hat{\Gamma}_{\text{in}}$ denotes the part of the interface where $\mathbf{u}_\infty \cdot \mathbf{n}_\Gamma < 0$, i.e., where the outer air hits the droplet. The assumption of neglecting all shear forces between the droplet and the air might be too unrealistic. Thus, via boundary layer theory it is possible to additionally add a shear force as boundary condition with a term like

$$f_{\text{shear}}(\mathbf{v}) = \int_{\hat{\Gamma}} J\frac{1}{\delta}\mathbf{P}_\Gamma \circ \mathbf{d}\mathbf{u}_\infty \cdot \mathbf{v} \, ds, \quad (6.36)$$

where δ refers to the boundary layer thickness, which might be defined by $\delta = (\text{Re}_{\text{loc}})^{-\frac{1}{2}}$, the local Reynolds number between the fluid and the air.

Evidence that this approach is indeed justified, will be given below based on numerical simulations of the full air and droplet simulations using the interface capturing approach. In a sense, this is also in line with the literature, where it has been numerically affirmed that vortices in the airflow appear to have little impact as they primarily form long time after the air stream impacts the droplet, see e.g., Seevaratnam et al. (2010).

The governing equations are discretized using the open source finite element packages NETGEN and NGSolve, see Schöberl (1997) and Schöberl (2014). In all following examples, a Taylor-Hood type pair of ansatz spaces $\mathbf{V}_h \subset \mathbf{V}$, $Q_h \subset Q$ is used, where the pressure is discretized with one polynomial order less than the velocity. For the deformation space $\mathbf{D}_h \subset \mathbf{D}$ the same polynomial order as for the velocity is considered. A first order time-stepping method is used, which treats all arising terms - except the convection and surface tension term - implicitly. The additional ALE terms, however, are all treated explicitly in order to avoid the computational expenses of a non-linear system. We point out, however, that consecutive experiments shall be understood as guidelines how to simulate problems of this kind. Adaptions concerning parameters, physical quantities etc. might be reasonable and

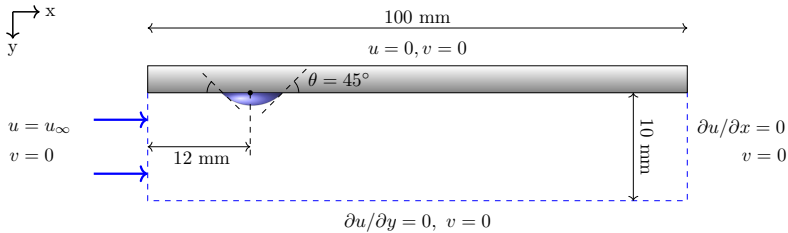


Figure 6.13: Case setup for 2D droplet simulations.

shall be adapted for each problem individually. As before, material parameters are described in Table 6.1 are used and the friction values in the effective wall and contact line forces are set as $\beta_L = \beta_s = 0.1$.

Numerical Results

We start with some two-dimensional examples in the interface-capturing approach, modeling the flow in both the air and the droplet. Results are compared with the observed droplet behaviour previous sections and the idea of unsteady oscillating airflow is explored. Afterwards, we omit the airflow and focus solely on the droplet behavior in two and three dimensions using the interface-tracking approach.

Interface-capturing simulations

The two-dimensional case setup for interface-capturing simulations is visualized in Figure 6.13. The top wall (i.e. the wafer) is treated with a no-slip condition, whereas the bottom boundary applies an impermeable free-slip condition. At the inlet, a uniform (but potentially time-varying) inlet velocity $u_\infty(t)$ is prescribed, and a zero-gradient Neumann condition is used as an outflow condition. The shape of the steady resting water droplet is obtained by initializing a half-circle of radius $r = 2$ mm at the top wall, and allowing it to relax by solving Equations (6.27)–(6.29) without any background airflow (i.e. $u_\infty = 0$ m/s).

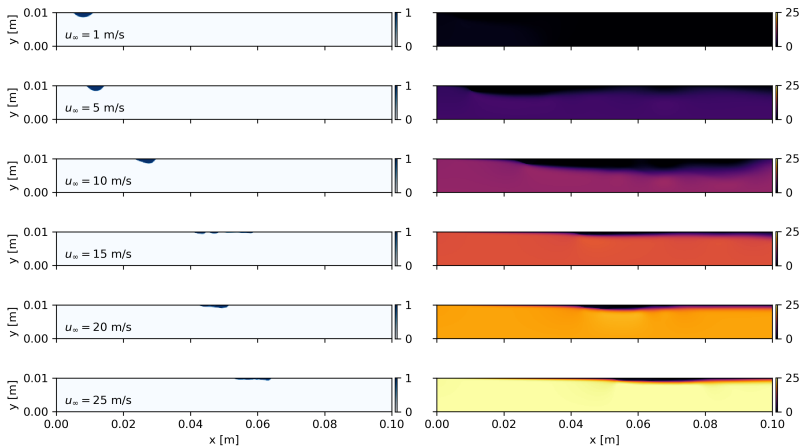


Figure 6.14: Snapshots at $t = 0.06$ s of water fraction α (left) and streamwise velocity u_x (right) for various inlet velocities u_∞ .

Steady inlet airflow $u_\infty(t)$ Firstly, we discuss the movement of the droplet as it is exposed to a uniform and steady inlet velocity. We define a total of six cases, i.e. with $u_\infty = 1, 5, 10, 15, 20,$ and 25 m/s.

Figure 6.14 illustrates snapshots of the water fraction and streamwise velocity for each value of u_∞ , 60 milliseconds after blowing is initiated. From the figure, it shows that the shape of and distance traveled by the droplets is highly dependent on u_∞ . Furthermore, the developing boundary layer has not yet transitioned to turbulence, even in the presence of the droplet obstacle.

A quantitative look at droplet movement is provided in Figure 6.15, where the position and speed of the droplets leftmost point of attachment to the wafer is plotted. The figure shows a number of observations. Firstly, it is observed that, for $u_\infty = 1$ m/s, there is no net movement of the droplet. Hence, there is a minimum threshold value for the driving airflow to initiate droplet movement. Second, droplets quickly attain a more-or-less steady terminal velocity, which increases as u_∞ increases. However, this increase is not linear, as can for instance be seen from

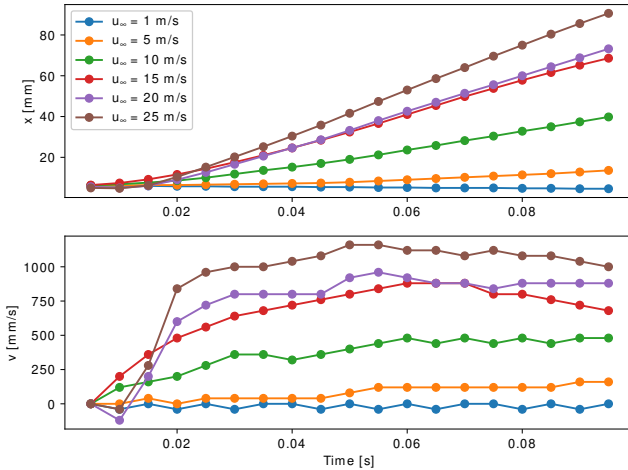


Figure 6.15: Position (top) and speed (bottom) of droplets for various inlet velocities u_∞ .

the similar behavior in the red and purple line at $u_\infty = 15$ and 20 m/s respectively. Finally, we see that for $u_\infty = 20$ and 25 m/s, the leftmost point of the droplet moves backwards first (negative velocity) before moving forward, which is not observed for any of the other moving droplet cases. This warrants further investigations into the dynamics of these cases.

The dynamics of the droplet shape can be further investigated from Figure 6.16. In this figure, the droplet shapes are visualized in a moving reference frame at $t = 0.03, 0.06,$ and 0.09 seconds after the initiation of blowing. Apart from the trivial, non-moving case at $u_\infty = 1$ m/s, three different regimes can be identified. Firstly, for $u_\infty = 5$ and 10 m/s, we see that the droplet shape does not vary much over time, and resembles the non-moving droplet shape, albeit with a significant asymmetry in the advancing and receding contact angles for the 10 m/s case. Secondly, at $u_\infty = 15$ m/s, damped oscillatory behavior of the

droplet shape occurs at a frequency of $f = 10 \dots 20$ Hz: initially part of the droplet is lifted from the wafer, then surface tension forces collapse it back to a flattened and segmented shape, after which part of the droplet is lifted anew to a lesser extent. This behavior is interesting, as the increase frontal area of the droplet could be an explanation for its somewhat higher than expected speed observed in previous paragraph. Third, for $u_\infty = 20$ and 25 m/s, the snapshots indicate a pancake-like squashed structure, similar to the shapes observed for high u_∞ in Section 6.2.2, which is subsequently driven by the shear stress with the airflow at its free surface. It is worth noting that this third regime is characterized by a fast transient related to the aforementioned negative initial velocity, not observed in Figure 6.16. Therefore, Figure 6.17 illustrates snapshots during the initial shape change of the droplet for $u_\infty = 25$ m/s shortly after the onset of blowing. It can be seen that the shape dynamics are akin to an aggravated version of the second regime described above, resulting in the ejection of small water droplets which are barely resolved by the grid. Shedding of such small droplets is highly undesirable. Similar ejection was observed in the case of $u_\infty = 20$ m/s, but not for any of the other cases. The current observations are consistent with the hypotheses of droplet breakup at higher velocities in Section 6.2.2.

Unsteady inlet airflow $u_\infty(t)$ Inspired by the high droplet speeds of the oscillating droplet shape at $u_\infty = 15$ m/s (i.e. the second regime discussed above), we attempt to improve droplet movement by applying an oscillating airflow $u_\infty(t)$ at the inlet. The inlet velocity is varied sinusoidally as $u_\infty(t) = U + A \sin(2\pi ft)$. As we aim to tap into similar dynamics as observed in the oscillating shape above, we use frequencies of 10 and 20 Hz. We use amplitudes A of 1 and 5 m/s, as well as an ‘amplitude’ of -5 to assess whether the phase of the sine wave is important. Finally, we limit ourselves to $U = 10$ and 15 m/s, as higher mean inlet velocities already break up the droplet as described above. This results in 12 additional simulations, in addition to the 4 simulations performed in the previous example.

The results of all simulations are summarized in Figure 6.18 and Table 6.2, which shows the droplet position after 100 ms, as well as its average velocity \bar{V} between 50 and 100 ms. A first observation is

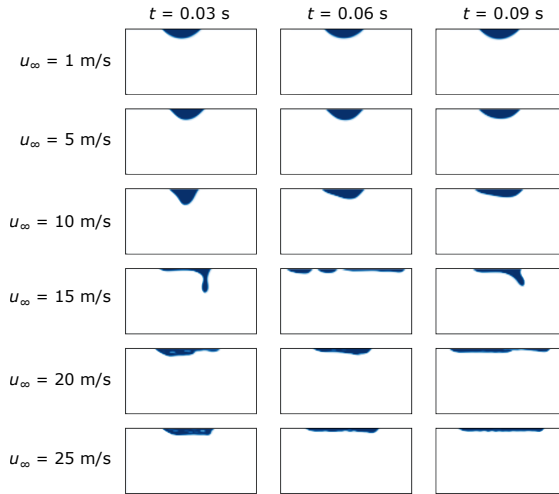


Figure 6.16: Droplet shapes in a moving reference frame at $t = 0.03, 0.06,$ and 0.09 seconds for each of the steady amplitude cases. Every box has the same width of 2 cm and height of 1 cm.

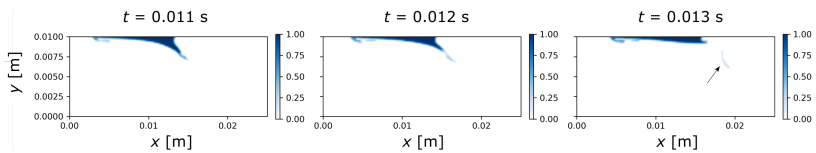


Figure 6.17: Droplet shapes for $u_\infty = 25$ m/s at $t = 0.011$ (left), 0.012 (middle), and 0.013 (right) seconds. The arrow in the latter panel indicates the shedding of a small under-resolved part from the main droplet.

that unsteadiness in the inlet can significantly increase both the droplet velocity, and hence its position after 10 ms, in comparison to the steady case with the same mean inlet. This can be observed, for instance, for case $(U, f, A) = (10 \text{ m/s}, 10 \text{ Hz}, 5 \text{ m/s})$ vs steady $U = 10 \text{ m/s}$. However, in these cases, the droplet still moves slower than in the steady case at the peak inlet value (i.e. $U = 15 \text{ m/s}$): unsteady blowing does not outperform simply increasing the baseline inlet airspeed. A second observation is that, for the unsteady cases with $U = 15 \text{ m/s}$ and $A > 0 \text{ m/s}$, instabilities cause the droplet to break up, which is highly undesirable. This can be omitted by phase-shifting the sine to initially reduce the airflow, but unfortunately this nullifies the observed increase in droplet movement, as seen for cases with $A < 0 \text{ m/s}$. In summary, for the current set of simulations, droplet movement cannot be enhanced by unsteady inlet airflow more than by just increasing the steady inlet airflow. From these results, we can conclude that the superior case, i.e. with highest droplet velocities without breakup, is at a steady $u_\infty = 15 \text{ m/s}$.

In summary, the 2D interface-capturing simulations seem to show sensible physical behavior: increasing the background airflow increases the droplet velocity but leads to breakup above 15 m/s. Unsteady droplet dynamics were observed in response to the initial onset of blowing. Unsteady blowing to tap into these dynamics however was unsuccessful based on the current cases. From the current results, blowing with a steady airflow of 15 m/s yields the maximal droplet velocity without breaking it into smaller pieces.

Given that current simulations still hold some simplifications, i.e. they are two-dimensional and spatial resolution is relatively coarse, we further consider the interface-tracking simulations at higher spatial resolutions in both two and three dimensions below.

Interface-tracking simulations

In the current simulations, we use the interface-tracking methodology detailed above to simulate the droplet behavior. As discussed earlier, in contrast to the interface-capturing simulations, we omit the explicit simulation of the airflow and impose the influence of the air on the droplet as a stress boundary condition. This omission is justified by

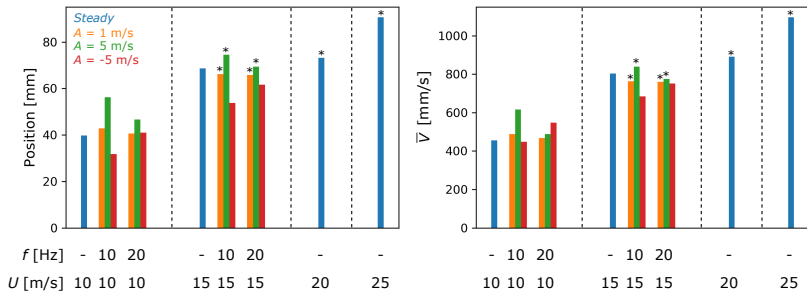


Figure 6.18: Droplet position after 100 ms (*left*) and time-averaged droplet velocity between 50 ms and 100 ms \bar{V} (*right*) for steady and unsteady inlet airflow cases. Colors depict the amplitudes of the sine waves, and * indicates cases where droplet breakup is observed.

Case			Observations		
U [m/s]	f [Hz]	A [m/s]	Position [mm]	\bar{V} [mm/s]	Droplet breakup
10	-	-	39.8	456	No
10	10	1	42.8	488	No
10	10	5	56.2	616	No
10	10	-5	31.8	448	No
10	20	1	40.6	468	No
10	20	5	46.6	488	No
10	20	-5	41.0	548	No
15	-	-	68.6	804	No
15	10	1	66.2	764	Yes, big droplets
15	10	5	74.6	840	Yes, big droplets
15	10	-5	53.8	684	No
15	20	1	65.8	760	Yes, big droplets
15	20	5	69.4	776	Yes, big droplets
15	20	-5	61.6	752	No
20	-	-	73.2	892	Yes, small droplets
25	-	-	90.6	1096	Yes, small droplets

Table 6.2: Numerical summary of steady and unsteady example cases, with inlet airflow $u_\infty(t) = U + A \sin(2\pi ft)$. Case with highest intact droplet velocities shown in bold.

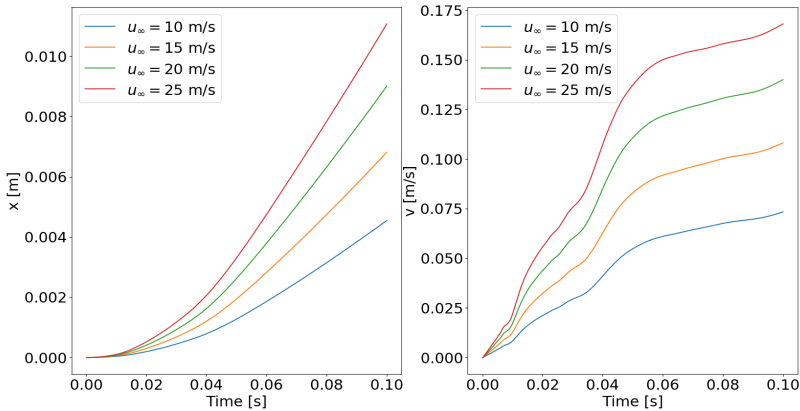


Figure 6.19: Position and velocity with respect to time for NGSolve example without air in 2D.

earlier observations, see e.g. Figure 6.14, where flow conditions upstream of the droplet were found to be laminar and homogeneous.

Two-dimensional droplet without air. Similar to the first simulations for the interface-capturing method, here we first consider two dimensional computations for different inflow velocities. Results can be found in Figure 6.19. The initial area of the droplet at $t = 0$ s is 16 mm^2 . We observe that the droplet's velocity is lower than the one obtained by the interface-tracking OpenFOAM simulations. The reason for this might be related to β_L as the solution behaves very sensitive to variations in this friction parameter. Further downstream, the wall would induce a thin boundary layer for the air, which is not considered here. The shape of the droplet is very stable, also for high velocities, see Figure 6.20. An explanation might be the neglected shear forces between the droplet and the air.

Three-dimensional droplet without air While computations of the full two-dimensional model (without elimination of the air) are challenging, but still reasonable, on standard machines, three-dimensional

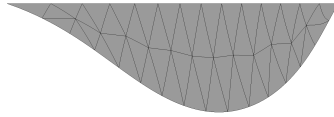


Figure 6.20: Shape of 2D droplet at $t = 0.1$ s for $u_\infty = 25$ m/s.

experiments exceed the capacity of most computers in terms of memory and processing power. Considerations from above however indicate how the computational expense of the model might be reduced significantly, while at the same time the accuracy of a three-dimensional model is preserved. To this end, we consider the three-dimensional droplet model without the air domain in the same manner as we have done this in the two-dimensional case.

We consider the three-dimensional case, where the initial volume of the droplet at $t = 0$ s is given by 3.8 mm^3 . As shown in Figure 6.21, its shape deforms less than in the 2D case, see Figure 6.19, due to the discrepancy of the volumes. Its position and velocity with respect to time for different air speeds are illustrated in Figure 6.21. We observe lower peak velocities than in the 2D simulation, which we believe to be mostly caused by the different volumes.

Based on the discrepancy between the interface-capturing and the interface-tracking simulations, it is evident that the proposed model itself might not be accurate enough to draw reliable conclusions for real world phenomena. There are several aspects that need to be taken into account to increase the credibility of the model to a reasonable level. As indicated by our results, shear forces might have essential impact on the droplet's behaviour and should therefore be incorporated. Moreover, the absence of boundary layers in our simulations might not be realistic enough to match reality. Together with more sophisticated time-stepping methods, these remarks should be embraced at the very first to improve the fidelity of consecutive simulations.

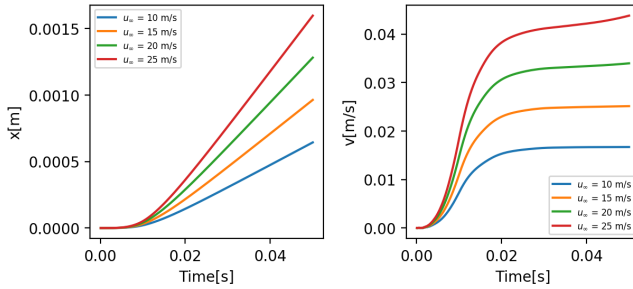


Figure 6.21: Position and velocity with respect to time for NGSolve example without air in 3D.



Figure 6.22: Shape of 3D droplet at $t = 0.05$ s for $u_\infty = 25$ m/s.

6.3 Discussion

A total of four modeling approaches were introduced in Section 6.2: a force-balance model (further denoted as FB), a Navier–Stokes model with the lubrication approximation (LUB), and two full Navier–Stokes models based on interface-capturing (NS-IC) and interface-tracking (NS-IT) respectively. In the current section we reiterate and compare the main findings, capabilities and limitations of these models.

In terms of computational cost there is a clear distinction between the ODE-based models FB and LUB on the one hand, and the PDE-based CFD models NS-IC and NS-IT on the other. Indeed, the former models can easily be run within a timeframe of seconds, whereas the latter require a timeframe in the order of an hour to run on a standard workstation. Although full three-dimensional CFD simulations would be feasible given additional time and parallel resources, within the current work the CFD models were rendered tractable by limiting the scope to two dimensions (NS-IC) or omitting the airflow (NS-IT).

A first observation from the flow field obtained from the NS-IC CFD model is that the air flow field is laminar and homogeneous at the point of interaction between the air and the droplet. This gives an initial justification for omitting the explicit detailed modeling of the airflow in LUB and NS-IT. It remains to be mentioned that further work is necessary to affirm the reliability of this model reduction in a credible way. Comparisons with high-fidelity three-dimensional CFD computations that incorporate the air domain as such are required to judge whether the impact of the elimination process is indeed as negligible with respect to turbulence as expected by the heuristics.

A qualitative comparison of the numerical results to indicative outcomes of experimental measurements in Figure 6.2 clearly showed that the FB model is inaccurate in the current formulation. This was attributed to the high sensitivity of droplet velocity to the effective shape of the droplet, which is not accurately accounted for in the FB model. This led to the investigation of models that are closer to the physical principles based on the Navier–Stokes equations. The LUB, NS-IC, and NS-IT models each yield droplet velocities within the same order of magnitude for similar input parameters, and are qualitatively consistent with experimental observations.

An interesting observation found in FB, NS-IC, and NS-IT is that the initial transient of the steady droplet when first impacted by a steady airflow are very fast: the terminal droplet velocity is reached soon, and in most cases, the shape of the droplet remains more or less constant once the droplet is moving. This justifies the traveling-wave assumption made in the LUB model. Another observation is that, above a threshold velocity $u_\infty = 20$ m/s, LUB and NS-IC predict a change in the droplet dynamics: part of the droplet is squashed into a very thin layer, which seems related to the highly undesirable breakup in to smaller droplets. This gives numerical evidence that simply blowing harder will not yield minimal droplet removal times.

The observation of an oscillating droplet shape in the NS-IC results at $u_\infty = 15$ m/s motivated the investigation of droplet blowing using sinusoidally varying airflows with a frequency of 10 and 20 Hz. Although this increased the droplet velocity in comparison to the steady case, there was no statistically significant improvement over the steady case with $u_\infty = 15$ m/s.

Even though qualitative comparison shows similarities between models, Quantitative comparison of the droplet velocities for the LUB, NS-IC and NS-IT models results in a significant difference. The LUB and NS-IT model which, in contrast to the NS-IC model, do not explicitly model the air flow, lead to significantly lower droplet velocities for similar setups. This indicates that current results and observations are indicative, and further work is necessary to assess the validity of the models, using both additional high-fidelity simulations and a dedicated experimental measurement setup.

6.4 Conclusion & Recommendation

In response to a problem statement of wafer contamination by VDL ETG, the current work investigates the modeling of airflow-driven water droplet removal from a flat wafer surface. Based on the complex flow physics of the problem at hand, a set of four models was developed, ranging in computational cost, fidelity and complexity.

A qualitative comparison between models yields similar observations. The flow physics are characterized by fast transients and, above

a threshold velocity, droplet shapes are highly altered and breakup occurs. Based on the current simulations of one of the CFD models based on an interface-capturing approach, unsteady blowing significantly impacts the droplet dynamics, yet for the current parametric study, the highest droplet velocities are observed for a steady airflow. This is however a first indication that unsteady blowing could prove favorable.

An important conclusion is that, although the models show qualitative similarities, attaining quantitative agreement between models is not attempted in this work. This is partly due to the lack of dedicated experimental data, and various assumptions and parameters included in the models. In the future, high-fidelity three-dimensional simulations and detailed controlled experiments should be used to tune the current models to provide the most reliable predictions possible. This work should be seen as conceptual guideline how prospective simulations can be performed at reasonable costs. In summary, we formulate the main findings of the current work into a set of three recommendations for future work:

Firstly, based on observations of the interface-capturing simulations, unsteady dynamics at specific frequencies excite specific response modes in the droplet shape that affect the droplet movement. It would be interesting to investigate droplet behavior experimentally under similar conditions.

Second, there is a lack of high-fidelity data for the specific task at hand. In that regard, we recommend a detailed and controlled experimental measurement setup, complemented with a high-fidelity three-dimensional CFD simulation including the background airflow for a specific condition, i.e. a specific droplet size with specific airflow. This will facilitate the validation and tuning of the models presented in this work.

Finally, we show that accurately modeling the physical behavior of the system is challenging and high-fidelity simulations of the unsimplified problem is computationally expensive. In response, we show here a chain of relatively inexpensive models that, after proper validation, can be used to explore removal strategies at a modest computational cost, e.g. for a variety of droplet sizes, airflow frequencies and amplitudes. The outcome of this could further guide the design of experimental measurements or high-fidelity simulations.

References

- Cox, R.G. (1986). “The dynamics of the spreading of liquids on a solid surface. Part 1. Viscous flow”. In: *Journal of Fluid Mechanics* 168, pp. 169–194.
- Deshpande, S.S., L. Anumolu, and M.F. Trujillo (Nov. 2012). “Evaluating the performance of the two-phase flow solver interFoam”. In: *Computational Science & Discovery* 5.1, p. 014016. DOI: 10.1088/1749-4699/5/1/014016.
- Ding, H. and P. Spelt (May 2007). “Wetting condition in diffuse interface simulations of contact line motion”. In: *Physical review. E, Statistical, nonlinear, and soft matter physics* 75, p. 046708. DOI: 10.1103/PhysRevE.75.046708.
- Donea, J. et al. (2004). “Arbitrary Lagrangian-Eulerian Methods”. In: *Encyclopaedia of Computational Mechanics*. John Wiley & Sons. Chap. 1.14.
- Fan, J., M.C.T. Wilson, and N. Kapur (2011). “Displacement of liquid droplets on a surface by a shearing air flow”. In: *Journal of Colloid and Interface Science* 356.1, pp. 286–292. ISSN: 0021-9797. DOI: <https://doi.org/10.1016/j.jcis.2010.12.087>.
- Fry, H. (Jan. 2011). “A Study of Droplet Deformation”. PhD thesis. University College London.
- Grinats, E.S. et al. (2019). “Droplet dynamics on a body surface in a gas flow”. In: *High Temperature* 57.2, pp. 246–252.
- Hirt, C.W. and B.D. Nichols (1981). “Volume of fluid (VOF) method for the dynamics of free boundaries”. In: *Journal of Computational Physics* 39.1, pp. 201–225.
- Reusken, A., X. Xu, and L. Zhang (Oct. 2015). “Finite element methods for a class of continuum models for immiscible flows with moving contact lines”. In: *International Journal for Numerical Methods in Fluids*. DOI: 10.1002/fld.4349.
- Schöberl, J. (1997). “NETGEN An advancing front 2D/3D-mesh generator based on abstract rules”. In: *Computing and Visualization in Science* 1, pp. 41–52. ISSN: 1432-9360.
- (2014). “C++11 Implementation of Finite Elements in NGSolve”. In.

Seevaratnam, G.K. et al. (Aug. 2010). “Laminar flow deformation of a droplet adhering to a wall in a channel”. In: *Chemical Engineering Science* 65, pp. 4523–4534. DOI: 10.1016/j.ces.2010.04.012.